Higher-order interactions induce chimera states in globally coupled oscillators

Zerong Guo [1], Zonghua Liu [1], Shuguang Guan [1,*], Charo I. del Genio [2,3,4,†], Stefano Boccaletti [3,5,6] and Jie Zhou [1,‡]

[1] *School of Physics and Electronic Science, East China Normal University, Shanghai 200062, China*

[2] *Institute of Smart Agriculture for Safe and Functional Foods and Supplements, Trakia University, Stara Zagora 6000, Bulgaria*

[3] *Institute of Interdisciplinary Intelligent Science, Ningbo University of Technology, Ningbo, China*

[4] *School of Mathematics, North University of China, Taiyuan 030051, China*

[5] *CNR—Institute of Complex Systems, Via Madonna del Piano 10, I-50019 Sesto Fiorentino, Italy*

[6] *Sino-Europe Complexity Science Center, North University of China, Taiyuan 030051, China*

(Received 2 June 2025; revised 13 November 2025; accepted 17 February 2026; published 2 April 2026)

We show that globally coupled phase oscillators inherently possess a phase frustration when four-body interactions are considered. This intrinsic frustration arises when oscillators have asymmetric distributions of initial conditions spanning across multiple fixed points. Moreover, when the frequency distribution is bimodal, the two groups of oscillators may evolve toward distinct macroscopic dynamical behaviors, with one group being synchronized and the other remaining asynchronous. This constitutes a mechanism for the emergence of chimera states, and one that is specifically characteristic of higher-order interactions.

DOI: 10.1103/bq1t-y92y

I. INTRODUCTION

Higher-order interactions, represented in a network structure by hyperedges or simplices, play a crucial role in a variety of complex systems, ranging from ecology [1,2] to social interactions [3–5] and neuroscience [6–8], introducing collective behaviors that cannot be captured by pairwise interactions alone [9–11]. In particular, theoretical and experimental results have shown that higher-order interactions have a significant impact on chimera states [12–18], a phenomenon characterized by the coexistence of multiple distinct domains [19,20]. Originally introduced in arrays of identical oscillators [19], the notion of chimera has been broadened and extended to more general settings [21–24], and chimera states have been observed in a variety of complex systems, including chemical [25,26], optical [27], neural [28], and electrical systems [29].

Recently, the attention of complexity scientists has focused on systems with interactions beyond pairwise ones, where many-body connections are known to induce a variety of characteristic behaviors [30–32]. Nonetheless, despite extensive research on the topic, the qualitative distinctions between the effects that can be ascribed to three-body interactions and those caused by interactions at even higher orders remain underexplored. For example, when analyzing the Kuramoto model, many studies focus on second-order (three-body) interactions, demonstrating that they can lead to phenomena that are qualitatively different from the pairwise case, such as multistability [33], chaos [34], abrupt desynchronization [35], secondary instabilities, and collective chaos [36], as well as anomalous transitions to synchrony [37]. Conversely, the landscape of research on interactions beyond the second order remains less developed. In fact, even when such interactions are taken into account [34,38], the coupling terms seldom reflect the multistability observed in the higher-order Kuramoto model, which stems from the presence of multiple fixed points [33,39,40], as often occurs in real-world systems [41–44]. As a result, there is little evidence for phenomena with respect to the second-order case.

In this article, we consider a natural generalization of the classic Kuramoto model with third-order (four-body) interactions, in which each oscillator has threee stable fixed points. We show that asymmetric initial conditions, as are often encountered in real-world systems [45–47], can induce a dynamical asymmetry even if the network topology and the natural frequency distribution of the oscillators are symmetric, introducing an effect on the system that is equivalent to that of frustration and does not occur under first- and second-order interactions alone. Because of this, and in analogy to biological systems [48], we call this phenomenon *intrinsic frustration*. Additionally, for a system with a symmetric bimodal frequency distribution, intrinsic frustration can break the symmetry and lead to the emergence of chimera states in which the oscillators with natural frequencies close to the two peaks exhibit different dynamical behavior. Finally, we derive the conditions for the formation of such chimeras using the Ott-Antonsen method [49,50]. Extensive numerical simulations reveal that this phenomenon is robust with respect to increases in the order of interaction, changes in the network topology, differences in the frequency distribution, and even the weaker lower-order couplings.

*Contact author: sgguan@phy.ecnu.edu.cn

†Contact author: charo.delgenio@trakia-uni.bg

‡Contact author: jzhou@phy.ecnu.edu.cn

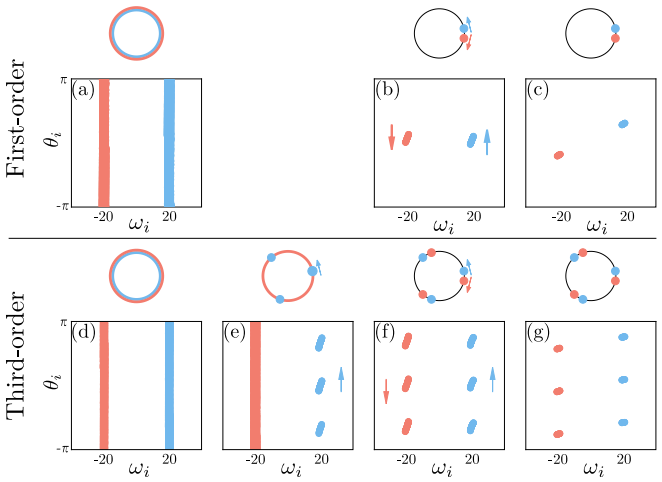

FIG. 1. Macroscopic phases of the Kuramoto model with a bimodal uniform natural frequency distribution. Top row: first-order Kuramoto model, with snapshots of the (a) incoherent ($K = 1$, $t = 21.451$), (b) standing-wave ($K = 10$, $t = 3.562$), and (c) synchronous ($K = 40$, $t = 1.080$) states. Bottom row: third-order Kuramoto model as defined in Eq. (1), with snapshots of the (d) incoherent ($K = 10$, $t = 54.775$), (e) chimera ($K = 20$, $t = 70.275$), (f) standing-wave ($K = 25$, $t = 3.562$), and (g) synchronous ($K = 50$, $t = 11.005$) states. Blue (red) points denote the phase of oscillators rotating in the positive (negative) direction. Schematic insets above each panel summarize the system state: Filled circles denote synchronized clusters and colored edges indicate incoherent oscillators with uniformly distributed phases. All panels show direct numerical simulations with $N = 10^4$ oscillators, integration time step 10^{-3}, and initial conditions placing 90% : 9% : 1% of oscillators at three phases separated by $2\pi/3$. Natural frequencies are drawn from a bimodal uniform distribution with peaks at $\pm\omega_0 = \pm 20$ and half-width $\Delta = 1$ per peak. In all cases, t denotes the snapshot time.

II. RESULTS

Consider an ensemble of N globally coupled oscillators. The phase θ_i of each oscillator satisfies

$$\dot{\theta}_i = \omega_i + \frac{K}{N^3} \sum_{j,k,l=1}^{N} \sin(\theta_j + \theta_k + \theta_l - 3\theta_i), \tag{1}$$

where ω_i is the natural frequency of the oscillator and K is the coupling strength of the four-body interactions. Note that the second term represents a four-body coupling that cannot be factorized into pairwise interactions. Also, we assume a bimodal distribution of natural frequencies. This type of distribution has been extensively studied in the classic Kuramoto model [51], in which oscillators transition from an incoherent state to a standing wave and then to a synchronous state as the coupling strength K increases. In the third-order model, however, an initially asymmetric phase distribution can give rise to a chimera state in which oscillators in one direction attain synchrony while those in the other direction remain unsynchronized, as illustrated in Fig. 1. Note that, as detailed in Appendix A, this phenomenon is observed independently from the choice of distribution.

To understand the mechanism by means of which higher-order interactions generate chimera states, start by introducing

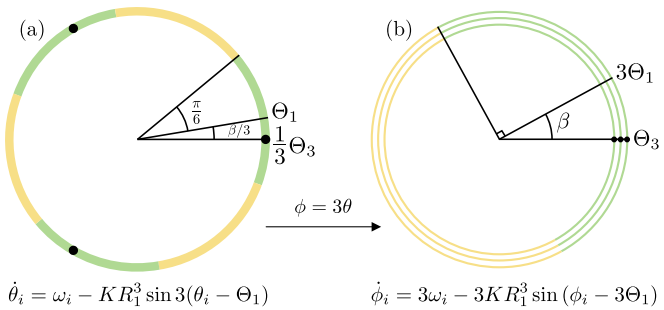

FIG. 2. Stable fixed points of the third-order Kuramoto model. (a) The black dots show the positions of the three fixed points of the oscillators, whose phases are 0, $\frac{2\pi}{3}$, and $\frac{4\pi}{3}$. The green regions represent the areas where the fixed points are stable, namely, $(\Theta_1 - \frac{5\pi}{6}, \Theta_1 - \frac{\pi}{2})$, $(\Theta_1 - \frac{\pi}{6}, \Theta_1 + \frac{\pi}{6})$, and $(\Theta_1 + \frac{\pi}{2}, \Theta_1 + \frac{5\pi}{6})$, where Θ_1 is the phase of the order parameter z_1. (b) After the scaling transformation $\phi_i = 3\theta_i$, the period of the oscillator phases increases from 2π to 6π, containing three 2π cycles. The phase of the order parameter in the new scale, Θ_1, is scaled to $3\Theta_1$, while Θ_3 is the phase of the order parameter in the new scale. The three fixed points of each oscillator collapse onto a single point, and the three stable regions also merge into one single region $(3\Theta_1 - \frac{\pi}{2}, 3\Theta_1 + \frac{\pi}{2})$.

the classic Kuramoto order parameter, which is the complex number $z_1 = R_1 e^{i\Theta_1} = \frac{1}{N}\sum_{j=1}^{N} e^{i\theta_j}$. Here, R_1 is the mean amplitude of the oscillators, which represents their degree of synchronization, and Θ_1 is their average phase. This allows one to rewrite Eq. (1) as

$$\dot{\theta}_i = \omega_i - KR_1^3 \sin(3(\theta_i - \Theta_1)). \tag{2}$$

To facilitate analysis, a corotating frame is used in which the frequency of the average phase Θ_1 is held constant. The fixed points of an oscillator with frequency ω_i can be determined by solving $\dot{\theta}_i = 0$, and they are stable if they lie within regions in which $\frac{d}{d\theta_i}\dot{\theta}_i < 0$. From Eq. (2), one can derive three stable fixed points

$$\theta_i^* = \Theta_1 + \frac{1}{3}\arcsin\frac{\omega_i}{KR_1^3} + \frac{2p\pi}{3}, \tag{3}$$

where $p \in \{0, 1, 2\}$ and $-KR_1^3 \leqslant \omega_i \leqslant KR_1^3$. Thus, the fixed points are separated by $\frac{2\pi}{3}$, as illustrated in Fig. 2(a). In the synchronous state, each oscillator settles on one of these three stable fixed points, depending on its initial conditions, resulting in the formation of three synchronized clusters.

Then, apply a scaling transformation $\phi_i = 3\theta_i$, after which the dynamical Eq. (2) becomes

$$\dot{\phi}_i = 3\omega_i - 3KR_1^3 \sin(\phi_i - 3\Theta_1), \tag{4}$$

and, in analogy to the first-order parameter z_1, define the third-order parameter in the new scale as

$$z_3 = \frac{1}{N}\sum_{j=1}^{N} e^{i\phi_j} = \frac{1}{N}\sum_{j=1}^{N} e^{3i\theta_j} = R_3 e^{i\Theta_3}. \tag{5}$$

In the transformed system, the three stable fixed points collapse onto a single position on the circle. This transformation effectively reduces the dynamics of the third-order Kuramoto model to a form similar to that of the classic one, thus simplifying its treatment.

Note that the phases of the first-order and third-order parameters are in general different. To see this, consider an ensemble of oscillators synchronized in the three stable regions in varying proportions γ_0, γ_1, and γ_2. Also, let the partial nth order parameter for the N_p oscillators in the pth stable region P be $z_{n,p} = R_{n,p}e^{i\Theta_{n,p}} = \frac{1}{N_p}\sum_{j\in P} e^{i\theta_j}$. If the oscillators have the same frequency distribution, their phase distributions in the stable regions are identical up to a constant phase shift of $\frac{2\pi}{3}$. This means that the partial nth order parameters in different regions have identical magnitudes $R_{n,p}$ and phase differences of $\frac{2n\pi}{3}$, where the factor of n is due to the scaling transformation. Therefore, using the definition of the first-order parameter, it is $z_1 = R_1 e^{i\Theta_1} = \sum_{p=0}^{2}\gamma_p z_{1,p} = \sum_{p=0}^{2}\gamma_p R_{1,p}e^{i(\frac{2p\pi}{3}+\Theta_{1,0})} = R_{1,0}e^{i\Theta_{1,0}}\sum_{p=0}^{2}\gamma_p e^{i\frac{2p\pi}{3}}$. But then, since the arguments on both sides are equal, using $\Theta_{1,0} \approx \frac{1}{3}\Theta_3$, the phase difference between the first-order and third-order parameters can be approximated as

$$\Theta_1 - \frac{1}{3}\Theta_3 = \arg\left(\sum_{p=0}^{2}\gamma_p e^{i\frac{2p\pi}{3}}\right). \tag{6}$$

It is evident that, if the fractions of oscillators in each region are all different, then $\Theta_1 \neq \frac{1}{3}\Theta_3$. Figure 2 illustrates this scenario, in the case of $\Theta_3 = 0$ and $\Theta_1 \neq 0$. In such situations, Θ_1 does not coincide with the center of the oscillators in any stable region. This is in stark contrast with the first-order Kuramoto model, where each oscillator has only one stable point, precluding the possibility of such asymmetries and causing Θ_1 to always coincide with the center of the oscillators in the stable region. In the second-order Kuramoto model, the symmetry between two opposing fixed points also prevents such an offset. It is only when the interactions are of the third or greater order that this symmetry-breaking effect appears.

Now, to make the relevance of the phase difference explicit, rewrite Eq. (4) as

$$\dot{\phi}_i = 3\omega_i - 3KR_1^3\sin\left((\phi_i - \Theta_3) - \beta\right), \tag{7}$$

where we have put $\beta = (3\Theta_1 - \Theta_3)$. This term represents the phase difference between the order parameters in the two scales, and it is analogous to the frustration term of the Kuramoto-Sakaguchi model [52]. However, unlike the externally imposed frustrations considered so far in the literature, β arises entirely from the intrinsic properties of the system, as its origin lies fundamentally within the asymmetry that is made possible by the higher-order interactions. Therefore, we call this difference term the *intrinsic frustration* of the third-order Kuramoto model. This intrinsic frustration arises specifically in models of the third order and greater, where the multiplicity of stable fixed points enables the dynamical asymmetry. Note that in systems with a unimodal frequency distribution, this frustration introduces a bias that causes the angular velocity of the order parameter to deviate from the average natural frequency of the oscillators, as detailed in Appendix A. For systems with a bimodal distribution, in the presence of intrinsic frustration, the symmetry of the synchronized clusters that rotate in opposite directions in the standing-wave state is broken, ultimately leading to the emergence of chimera states. To understand the mechanism of this symmetry breaking, examine the dynamical processes occurring in the system in the standing-wave state. Here, the direction in which each oscillator rotates is determined by which peak in the frequency distribution is closer to its natural frequency. Then, the oscillators rotating in each direction split into three separate clusters. Consider now the largest synchronized cluster in both directions and approximate the phases of the oscillators within them as being all equal to their mean θ. Then, assuming that an oscillator is affected by an infinitesimal perturbation, its variation in velocity can be expressed from Eq. (2) as

$$\frac{\mathrm{d}}{\mathrm{d}\theta_i}\dot{\theta}_i = -3KR_1^3\cos\left(3(\theta - \Theta_1)\right). \tag{8}$$

When $\frac{\mathrm{d}}{\mathrm{d}\theta_i}\dot{\theta}_i < 0$, i.e., when $\theta \in (\Theta_1 - \frac{\pi}{6}, \Theta_1 + \frac{\pi}{6})$, the oscillators move closer together, and this range identifies a convergence region. Conversely, outside of this range, the oscillators are in a divergence region, moving away from each other.

When $\beta = 0$, the center of the convergence region coincides with the center of the two clusters, as shown in Fig. 3(a). However, when $\beta \neq 0$, the two centers become misaligned, causing the oscillators in two directions to enter and exit the regions at different times, as illustrated in Fig. 3(b). The relationship between velocity and phase, shown in Figs. 3(c) and 3(d) and explicitly derived in Appendix B, causes the synchronized cluster to move more slowly through the region of positive phases than through that of negative ones. This

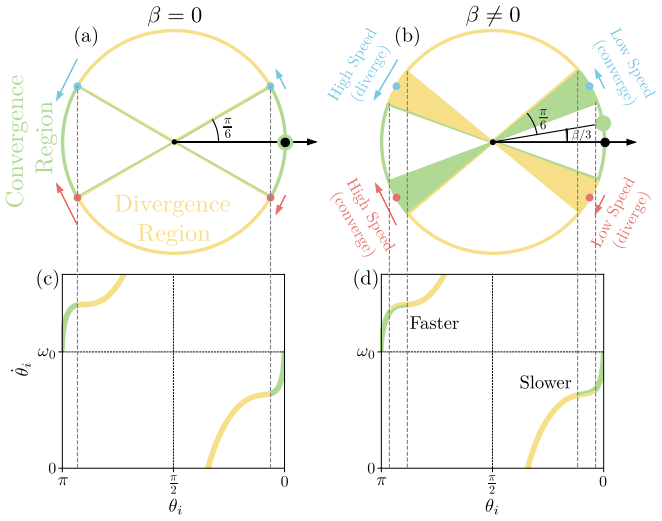

FIG. 3. Intrinsic frustration causes dynamical symmetry breaking. (a), (b) Qualitative changes in the dynamics of synchronized clusters in the third-order Kuramoto model caused by intrinsic frustration. The blue and red points represent the synchronized clusters of oscillators rotating in the positive and negative directions, respectively, both starting from $\theta = 0$. The green (orange) areas represent convergence (divergence) regions, where oscillators gradually converge (diverge). The pairs of dashed lines in panel (b) indicate areas where the stability of the two directions of the clusters differs. Intrinsic frustration causes the center of the convergence region (green point) to differ from the the center of the oscillators (black point). (c), (d) The relationship between the velocity of the oscillators $\dot{\theta}$ and their phase θ causes the time spent in the convergence and divergence regions to depend on the direction of rotation in the presence of intrinsic frustration.

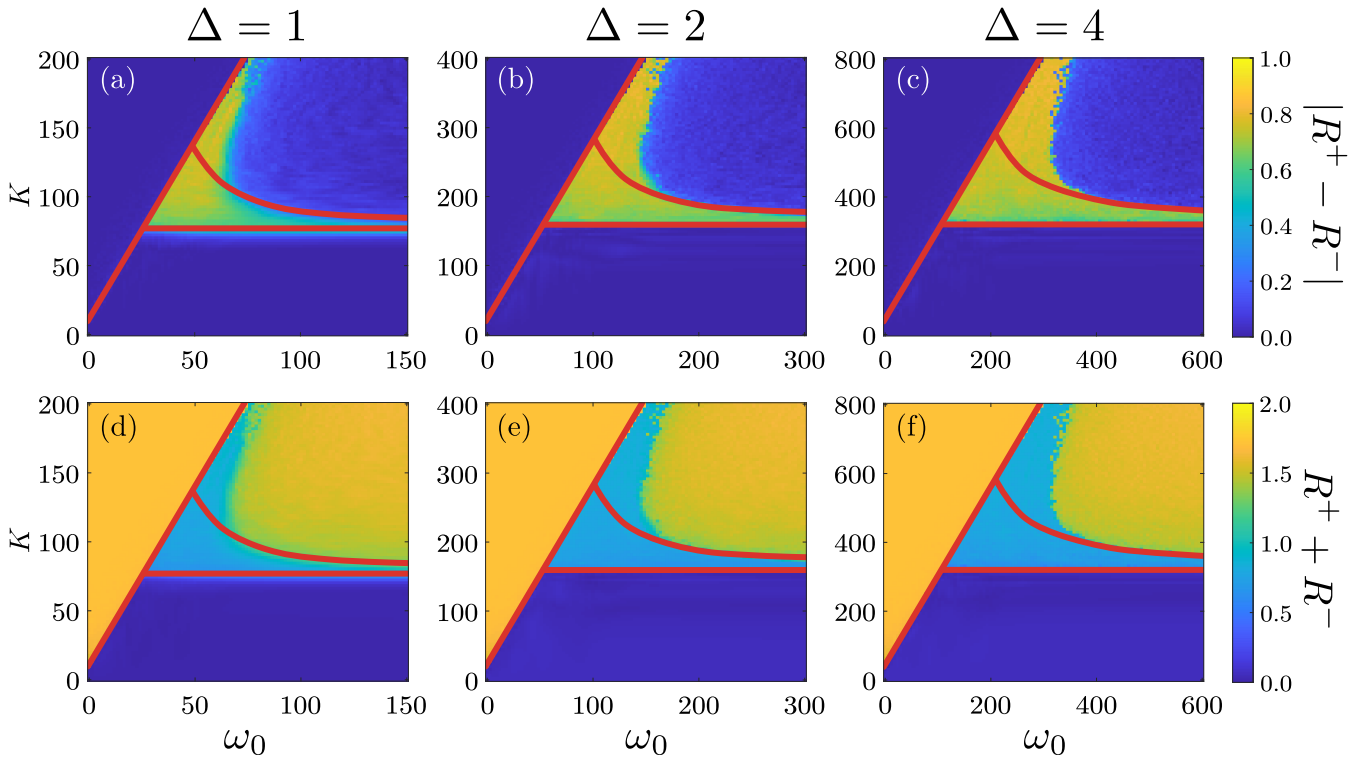

FIG. 4. Intrinsic frustration induces chimeras in higher-order dynamical networks. In all panels, the horizontal axis is ω_0, and the vertical axis is the coupling strength K. (a)–(c) The absolute value of the difference between the partial order parameter for positive-rotating oscillators, R^+, and that for negative-rotating ones, R^- directly reflects the difference in synchronization state between the two groups. In the chimera state, the positive-rotating group is synchronized (R^+ is high), while the other remains asynchronous (R^- is low), resulting in a high value of $|R^+ - R^-|$ that clearly outlines the chimera region. (d)–(f) In the unsynchronized state (lower part of the diagram) both R^+ and R^- are close to 0, as is their sum (dark blue). In the synchronous state (left part of the diagram) and in the standing wave one (right part of the diagram), both groups are highly synchronized, resulting in higher values of $R^+ + R^-$ (yellow). In the chimera state (central part of the diagram), one group is synchronized, while the other is not, yielding an intermediate value of $R^+ + R^-$ (light blue). All colored panels are obtained from numerical simulations of Eq. (2) with $N = 1000$ oscillators, integration time step 10^{-3}, and total simulation time $t = 20$. The red curves show the analytical boundaries computed from Eq. (10) by numerical integration with $\Delta t = 10^{-5}$ and $t = 10$, demonstrating a good agreement between theory and simulations.

results in the positive-rotating cluster spending a longer time in the convergence region than in the divergence one. Additionally, the speeds of the oscillators are independent from the direction of rotation. Consequently, the negative-rotating cluster has the opposite phenomenology to the positive-rotating one, spending more time in the divergence region than in the convergence one. Therefore, if the standing-wave state is unstable, the negative-rotating cluster will be the first to diverge into an asynchronous state, while the positive-rotating one may remain synchronized, leading to the formation of a chimera state.

To determine the conditions for the appearance of the chimera state, we apply the dimensionality reduction method proposed by Ott and Antonsen [49,50]. For this analysis, we assume that the bimodal distribution of natural frequencies is given by the sum of two Lorentzian distributions,

$$g_{\omega_0}(\omega) = \frac{\Delta}{2\pi}\left(\frac{1}{(\omega-\omega_0)^2+\Delta^2} + \frac{1}{(\omega+\omega_0)^2+\Delta^2}\right), \quad (9)$$

where Δ is the half-width at half maximum of each Lorentzian and $\pm\omega_0$ are their peak frequencies. This yields a low-dimensional system that governs the dynamics via the order parameters z_1 and z_3 (see Appendix C for details). The resulting equations are

$$\begin{aligned}\dot{z}_{3+} &= -\frac{3K}{2}\left(z_1^{*3}z_{3+}^2 - z_1^3\right) - 3(\Delta - \mathrm{i}\omega_0)z_{3+},\\ \dot{z}_{3-} &= -\frac{3K}{2}\left(z_1^{*3}z_{3-}^2 - z_1^3\right) - 3(\Delta + \mathrm{i}\omega_0)z_{3-},\end{aligned} \quad (10)$$

where z_{3+} and z_{3-} represent the partial third-order parameters of the positively and negatively rotating oscillators, respectively, and they satisfy $z_3 = (z_{3+} + z_{3-})/2$. To solve the system above, we require a relation between z_1 and z_3, which we obtain partly analytically and partly numerically from a stable correspondence between the partial order parameters $z_{1,p}$ and $z_{3,p}$ (see Appendix D for details). Solving the system in Eq. (10), we can then predict the boundaries of the four regions we expect, namely, the synchronous one, the asynchronous one, the standing-wave, and the chimera state. Then, having obtained a full phase diagram, we simulate the system directly and compare the theoretical predictions with the simulation results, as illustrated in Fig. 4. The results show a good agreement between theory and simulations. In fact,

the boundary between the chimera state and the standing-wave state, represented by the red curve separating the central region and the upper-right one, shows an excellent correspondence for large ω_0. Nonetheless, some discrepancies emerge for lower values. These can be explained by noting that in the standing-wave state, each synchronous cluster oscillates between convergence and divergence regions. When a cluster enters a divergence region, some of its oscillators may leave their original stable region and join another, thereby altering the ratios between γ_0, γ_1, and γ_2. This effect is particularly pronounced when ω_0 is smaller, as clusters spend more time in the divergence regions, thereby increasing the likelihood of ratio changes. Since our theoretical calculations assume that these ratios remain constant, we conjecture that this mechanism accounts for a sizable part of the observed discrepancy. At the same time, we would like to stress that our main result is the very existence of a mechanism for the emergence of a chimera state, rather than an analytical description of its boundaries that holds for any value of the dynamical parameters. The bifurcations corresponding to the phase boundaries are further analyzed in Appendix E.

III. DISCUSSION

Beyond the specific examples discussed above, intrinsic frustration exerts a profound influence on system dynamics in more general settings. For instance, chimera states persist in Kuramoto models of order higher than three and are robust with respect to the presence of weak first- or second-order couplings. This phenomenon is not confined to globally coupled networks either, as it also emerges in random networks and brain-structural ones. Furthermore, the necessary dynamical asymmetry is not limited to an uneven distribution among a few fixed points but can also arise from imbalances across multiple coherent regions. These findings collectively establish the additional asymmetry induced by intrinsic frustration as a fundamental feature of higher-order complex networks. The numerical simulation supporting these findings is presented in Appendixes F–H.

In summary, we presented a mechanism to induce the appearance of chimera states in the third-order Kuramoto model. This is a true higher-order effect, as it is caused by the ability of interactions of order greater than 2 to introduce inherent asymmetries that are absent when considering only first- or second-order ones, and which originate from intrinsic frustration. In particular, we show how, when the natural frequencies of the oscillators are bimodally distributed, intrinsic frustration can disrupt their symmetry, causing oscillators with frequencies close to the two peaks to exhibit distinct dynamical behaviors, giving rise to a chimera. This phenomenon is not found in pairwise models or pure triadic ones, which instead preserve the dynamical symmetry of frequency-symmetric ensembles. Consequently, intrinsic frustration is essential to understand the collective dynamics of higher-order coupled systems.

ACKNOWLEDGMENTS

Z.G. acknowledges funding from the China Scholarship Council. Z.L. acknowledges STI2030-Major Projects 2021ZD0202600. C.I.D.G. acknowledges funding from the Bulgarian Ministry of Education and Science, under Project No. BG-RRP-2.004-0006-C02. J.Z. acknowledges the National Natural Science Foundation of China under Grant No. 12075088 and the Natural Science Foundation of Chongqing under Grant No. CSTB2024NSCQ-MSX0854.

DATA AVAILABILITY

The data that support the findings of this article are openly available [53].

APPENDIX A: DIFFERENT FREQUENCY DISTRIBUTIONS

1. Bimodal Gaussian and bimodal uniform distributions

For analytical clarity, we used above a bimodal Lorentzian frequency distribution to derive an Ott-Antonsen low-dimensional reduction of the model. To assess the robustness of the results, we carried out simulations replacing each Lorentzian peak with Gaussian and uniform components of comparable width. Notice that, as reported in Fig. 1, we already know that the uniform distribution still gives rise to the chimera state.

Specifically, the functional forms of the distributions we considered are

$$g_{\mathrm{G}}(\omega) = \frac{1}{2}\left[\frac{1}{\sqrt{2\pi}\,\Delta} e^{-\frac{(\omega-\omega_0)^2}{2\Delta^2}} + \frac{1}{\sqrt{2\pi}\,\Delta} e^{-\frac{(\omega+\omega_0)^2}{2\Delta^2}}\right] \tag{A1}$$

for the Gaussian frequencies and

$$g_{\mathrm{U}}(\omega) = \frac{1}{4\Delta}\left[\mathbf{1}_{\{|\omega-\omega_0|\leqslant\Delta\}} + \mathbf{1}_{\{|\omega+\omega_0|\leqslant\Delta\}}\right] \tag{A2}$$

for the uniform ones. In both cases, Δ controls the width of each peak and $\mathbf{1}$ is the indicator function. The chimera state is observed for both distributions, as shown in the phase diagrams illustrated in Fig. 5.

2. Symmetric unimodal distribution

We have seen that, in the bimodal case, the asymmetry of the initial phase distribution induces a chimera state. However, a form of dynamical asymmetry also appears for symmetric unimodal populations. To illustrate this, we consider the mean-field form of the nth-order Kuramoto model

$$\dot{\theta}_i = \omega_i - K_n R^n \sin(n(\theta_i - \Theta)) \tag{A3}$$

under a symmetric unimodal Lorentzian frequency distribution $g(\omega)$ with vanishing mean, width $\Delta = 1$, and initial phases placed at 0, $2\pi/3$, and $4\pi/3$ with population ratio $9:1:0$. Then, we vary the coupling strength K_n and measure the collective rotation rate $\Omega = \frac{\mathrm{d}}{\mathrm{dt}} \arg z$, where $z = Re^{\mathrm{i}\Theta} = \frac{1}{N}\sum_j e^{\mathrm{i}\theta_j}$. To avoid ill-defined phases, we only consider Ω when the magnitude of the order parameter satisfies $|z| \geqslant 0.1$. As shown in Fig. 6, we find that in the first- and second-order Kuramoto models ($n = 1$ or $n = 2$), at steady state, $\Omega \approx 0$. Conversely, for Kuramoto models of order higher than 2 ($n = 3$ and $n = 4$), the collective frequency satisfies $\Omega \neq \langle\omega\rangle = 0$, so that the system develops a dynamical

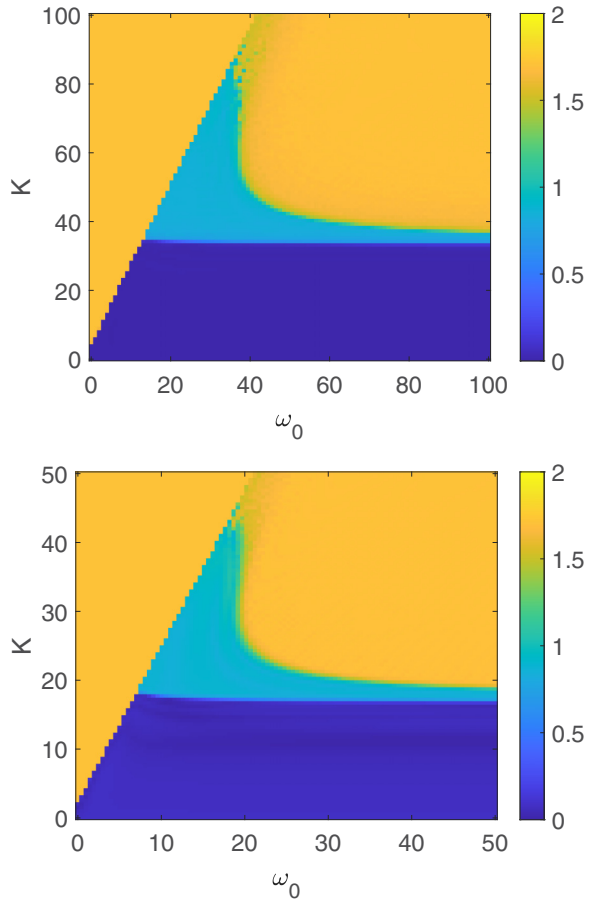

FIG. 5. The chimera state induced by intrinsic frustration also arises for bimodal Gaussian and bimodal uniform frequency distributions. The values of $R^+ + R^-$ at steady state show the chimera state emerging when the frequency distribution of the oscillators is bimodal Gaussian (left) and bimodal uniform (right). Both panels show the state of the system at time $T = 20$. The simulations used 1000 oscillators, integration step 10^{-4}, peak width $\Delta = 1$, and initial phases set at 0, $2\pi/3$, and $4\pi/3$ with population ratio $9 : 1 : 0$.

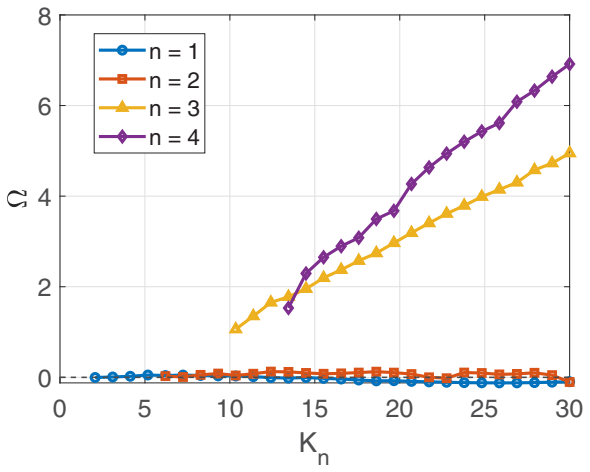

FIG. 6. Dynamical asymmetry arises in higher-order models also with unimodal frequency distributions. The angular velocity Ω of the order parameter at steady state is different from 0 in systems with order of interaction n greater than or equal to 3, but it vanishes for first-order and second-order models. The simulations used 1000 oscillators, integration step 10^{-3}, symmetric unimodal Lorentzian frequency distribution with vanishing mean and width $\Delta = 1$, and initial phases placed at 0, $2\pi/3$, and $4\pi/3$ with population ratio $9 : 1 : 0$. The value of Ω is estimated from the last 30% of the simulation trajectory.

asymmetry despite the symmetry of $g(\omega)$. These results show that, even with a symmetric unimodal frequency distribution, an asymmetry in the initial phase distribution can induce dynamical asymmetry for interaction orders greater than, whereas the corresponding lower-order models retain the dynamical symmetry.

APPENDIX B: VELOCITY-PHASE RELATION

To derive the relation between velocity and phase of the oscillators in the standing-wave state, start by noticing that, in the reference frame chosen, a vanishing phase corresponds to the center of the two synchronous clusters. This position differs from the average phase Θ_1 of the system by a constant, which means that the angular velocity of the reference frame is equal to the angular velocity Ω_1 of the average phase of the system.

To compute Ω_1, consider the definition of order parameter, which we rewrite here for convenience:

$$z_1 = R_1 e^{i\Theta_1} = \frac{1}{N}\sum_{j=1}^{N} e^{i\theta_j}. \tag{B1}$$

Differentiating this equation, we get

$$\dot{z}_1 = \dot{R}_1 e^{i\Theta_1} + iR_1 e^{i\Theta_1}\dot{\Theta}_1 = \frac{1}{N}\sum_{j=1}^{N} ie^{i\theta_j}\dot{\theta}_j, \tag{B2}$$

which we can solve for $\dot{\Theta}_1$ obtaining

$$\dot{\Theta}_1 = i\frac{\dot{R}_1}{R_1} + \frac{1}{NR_1}\sum_{j=1}^{N} e^{i(\theta_j-\Theta_1)}\dot{\theta}_j. \tag{B3}$$

However, the angular velocity $\dot{\Theta}_1$ is a real quantity. In turn, the first term in the right-hand side of the equation above is purely imaginary. Thus, we can write

$$\begin{aligned}\Omega_1 = \dot{\Theta}_1 &= \Re\dot{\Theta}_1 \\ &= \frac{1}{NR_1}\sum_{j=1}^{N}\Re(e^{i(\theta_j-\Theta_1)})\dot{\theta}_j \\ &= \frac{1}{NR_1}\sum_{j=1}^{N}\cos(\theta_j-\Theta_1)\dot{\theta}_j.\end{aligned} \tag{B4}$$

In the approximation we use, the oscillators in each synchronization cluster have the same phase, and, in the reference frame chosen, the phases of two clusters are on the opposite

of the other. Then, indicating the phases of the clusters with θ and $-\theta$, the equation above can be rewritten as

$$\begin{aligned}\Omega_1 &= \frac{1}{NR_1}\left(\sum_{j=1}^{\frac{N}{2}}\cos(\theta-\Theta_1)\dot{\theta}_j\big|_{\theta_j=\theta}+\sum_{j=\frac{N}{2}+1}^{N}\cos(-\theta-\Theta_1)\dot{\theta}_j\big|_{\theta_j=-\theta}\right)\\ &= \frac{1}{NR_1}\left\{\frac{N}{2}\cos(\theta-\Theta_1)\big[\omega_0-KR_1^3\sin(3(\theta-\Theta_1))\big]+\frac{N}{2}\cos(-\theta-\Theta_1)\big[\omega_0-KR_1^3\sin(3(-\theta-\Theta_1))\big]\right\}\\ &= \frac{1}{2R_1}\big\{\omega_0[\cos((\theta-\Theta_1)+\cos(\theta+\Theta_1)]-KR_1^3[\cos(\theta-\Theta_1)\sin(3(\theta-\Theta_1))-\cos(\theta+\Theta_1)\sin(3(\theta+\Theta_1))]\big\},\end{aligned} \tag{B5}$$

where we have used Eq. (2). Note that, with our assumptions, the partial order parameter of the oscillators in each region is proportional to $\cos\theta$. Thus, we can write $R_1 = R\cos\theta$, rewrite the equation for Ω_1 as

$$\begin{aligned}\Omega_1 = \frac{1}{2R\cos\theta}\{&\omega_0[\cos((\theta-\Theta_1)+\cos(\theta+\Theta_1)]\\ &-KR^3\cos^3\theta[\cos(\theta-\Theta_1)\sin(3(\theta-\Theta_1))-\cos(\theta+\Theta_1)\sin(3(\theta+\Theta_1))]\big\},\end{aligned} \tag{B6}$$

and compute the angular velocity of the synchronized group rotating in the positive direction as

$$\omega_i' = \dot{\theta}_i - \Omega_1 = \omega_0 - KR^3\cos^3\theta\sin(3(\theta-\Theta_1)) - \Omega_1. \tag{B7}$$

This relation is illustrated in Fig. 3. Note that the angular velocity of the negatively rotating synchronous cluster is the opposite of the angular velocity of the positively rotating one.

APPENDIX C: OTT-ANTONSEN APPROXIMATION EQUATIONS

1. Evolution of θ_i in terms of z_1

To apply the Ott-Antonsen method, we need to obtain a few auxiliary results. The first is a rewriting of Eq. (2), which we start as

$$\begin{aligned}\dot{\theta}_i &= \omega_i + KR_1^3\Im\left(e^{i(3\Theta_1-3\theta_i)}\right)\\ &= \omega_i + KR_1^3\frac{e^{i(3\Theta_1-3\theta_i)}-e^{-i(3\Theta_1-3\theta_i)}}{2i}.\end{aligned} \tag{C1}$$

Now, from Eq. (B1), using the fact that R_1 is real, we obtain

$$R_1 = z_1 e^{-i\Theta_1} = z_1^* e^{i\Theta_1}, \tag{C2}$$

where $*$ indicates complex conjugation. Then, substituting these expressions into the previous equation, we get

$$\dot{\theta}_i = \omega_i + \frac{K}{2i}\left[z_1^3 e^{i(-3\theta_i)} - z_1^{*3} e^{i(3\theta_i)}\right]. \tag{C3}$$

2. Density function

Next, we consider the system in the limit of a very large number of oscillators. In this regime, we can approximate the distribution of oscillators with a continuous formalism, introducing a function $f(\theta,\omega,t)$ that describes the density of oscillators with phase within an infinitesimal interval centered on θ and natural frequency within an infinitesimal interval centered on ω. To proceed, write f as a Fourier series,

$$f(\theta,\omega,t) = \frac{g(\omega)}{2\pi}\left(1+\sum_{n=1}^{\infty}\hat{f}_n(\omega,t)e^{in\theta}+\hat{f}_n^*(\omega,t)e^{-in\theta}\right), \tag{C4}$$

where $g(\omega)$ is the distribution of natural frequencies of the oscillators. Further, decompose f into symmetric and asymmetric components with respect to a $\frac{2\pi}{3}$ periodicity, so that

$$f(\theta,\omega,t) = f_s(\theta,\omega,t) + f_a(\theta,\omega,t), \tag{C5}$$

and the symmetric component satisfies

$$f_s(\theta,\omega,t) = f_s\left(\theta+\frac{2\pi}{3},\omega,t\right). \tag{C6}$$

Note that this implies that the symmetric component is given by the Fourier modes that are integer multiples of 3, so that

$$\begin{aligned}f_s(\theta,\omega,t) = &\frac{g(\omega)}{2\pi}\\ &\times\left(1+\sum_{m=1}^{\infty}\hat{f}_{3m}(\omega,t)e^{3im\theta}+\hat{f}_{3m}^*(\omega,t)e^{-3im\theta}\right).\end{aligned} \tag{C7}$$

Finally, make the ansatz that each Fourier coefficient whose index is a multiple of 3 decays geometrically:

$$\hat{f}_{3m}(\omega,t) = a^m(\omega,t). \tag{C8}$$

3. Continuity equation

Because the number of oscillators is conserved, f must satisfy the continuity equation

$$\dot{f} + \frac{\partial}{\partial\theta}(f\dot{\theta}) = 0. \tag{C9}$$

To solve it, we compute each term individually. Using Eq. (C4), the first one is

$$\dot{f} = \frac{g(\omega)}{2\pi}\left(1 + \sum_{n=1}^{\infty} \frac{\partial}{\partial \mathrm{t}}\left(\hat{f}_n(\omega,t)\mathrm{e}^{\mathrm{i}n\theta} + \hat{f}_n^*(\omega,t)\mathrm{e}^{-\mathrm{i}n\theta}\right)\right), \tag{C10}$$

$$\frac{\partial}{\partial\theta}\left(f\dot{\theta}\right) = \frac{\partial}{\partial\theta}\left(\frac{g(\omega)}{2\pi}\left(1 + \sum_{n=1}^{\infty} \hat{f}_n(\omega,t)\mathrm{e}^{\mathrm{i}n\theta} + \hat{f}_n^*(\omega,t)\mathrm{e}^{-\mathrm{i}n\theta}\right)\left\{\omega + \frac{K}{2\mathrm{i}}\left[z_1^3\mathrm{e}^{\mathrm{i}(-3\theta)} - z_1^{*3}\mathrm{e}^{\mathrm{i}(3\theta)}\right]\right\}\right), \tag{C12}$$

where we have used Eq. (C3). Now, note that the function being differentiated in the equation above is a combination of terms in $\mathrm{e}^{\mathrm{i}n\theta}$. Specifically, the coefficient of the generic $\mathrm{e}^{3\mathrm{i}m\theta}$ term is $\omega\hat{f}_{3m} + \frac{K}{2\mathrm{i}}z_1^3\hat{f}_{3m+3} - \frac{K}{2\mathrm{i}}z_1^{*3}\hat{f}_{3m-3}$, which, because of the ansatz in Eq. (C8), becomes $\omega a^m + \frac{K}{2\mathrm{i}}z_1^3 a^{m+1} - \frac{K}{2\mathrm{i}}z_1^{*3}a^{m-1}$. Thus, the derivative of the $\mathrm{e}^{3\mathrm{i}m\theta}$ term with respect to θ is

$$3\mathrm{i}m\left(\omega a^m + \frac{K}{2\mathrm{i}}z_1^3 a^{m+1} - \frac{K}{2\mathrm{i}}z_1^{*3}a^{m-1}\right)\mathrm{e}^{3\mathrm{i}m\theta}. \tag{C13}$$

The continuity equation in Eq. (C9) requires the sum of all the coefficients of equal powers to vanish. This is true in particular for the total coefficients of all the $\mathrm{e}^{3\mathrm{i}m\theta}$ terms. Thus, we have

$$ma^{m-1}\dot{a} + 3\mathrm{i}m\left(\omega a^m + \frac{K}{2\mathrm{i}}z_1^3 a^{m+1} - \frac{K}{2\mathrm{i}}z_1^{*3}a^{m-1}\right) = 0, \tag{C14}$$

which implies

$$\dot{a} + 3\mathrm{i}\omega a + \frac{3K}{2}z_1^3 a^2 - \frac{3K}{2}z_1^{*3} = 0. \tag{C15}$$

4. The third-order parameter

In the continuum approximation, the third-order parameter z_3 can be expressed as

$$z_3 = \int_0^{2\pi}\int_{-\infty}^{\infty} f(\theta,\omega,t)\,\mathrm{d}\,\omega\mathrm{e}^{3\mathrm{i}\theta}\,\mathrm{d}\theta = \int_0^{2\pi}\int_{-\infty}^{\infty}\frac{g(\omega)}{2\pi}\left(1 + \sum_{n=1}^{\infty}\hat{f}_n(\omega,t)\mathrm{e}^{\mathrm{i}n\theta} + \hat{f}_n^*(\omega,t)\,\mathrm{d}\,\omega\mathrm{e}^{-\mathrm{i}n\theta}\right)\mathrm{e}^{3\mathrm{i}\theta}\,\mathrm{d}\theta, \tag{C16}$$

where we have used Eq. (C4). However, the integral $\int_0^{2\pi}\mathrm{e}^{\mathrm{i}n\theta}\,\mathrm{d}\theta$ always vanishes except when $n = 0$, in which case its result is 2π. Thus, the equation above reduces to

$$z_3 = \int_0^{2\pi}\int_{-\infty}^{\infty}\frac{g(\omega)}{2\pi}\left(\hat{f}_3^*(\omega,t)\mathrm{e}^{-3\mathrm{i}\theta}\right)\mathrm{d}\,\omega\mathrm{e}^{3\mathrm{i}\theta}\,\mathrm{d}\theta = \int_{-\infty}^{\infty} g(\omega)a^*(\omega,t)\,\mathrm{d}\omega, \tag{C17}$$

where we have used Eq. (C8). In our model, we assume a bimodal distribution of natural frequencies given by the sum of two Lorentzians, with the peaks at $\pm\omega_0$ and half-width at half maximum Δ. This distribution, given by Eq. (9), can be rewritten as

$$g_{\omega_0}(\omega) = \frac{1}{4\pi\mathrm{i}}\left[\frac{1}{(\omega-\omega_0)-\mathrm{i}\Delta} - \frac{1}{(\omega-\omega_0)+\mathrm{i}\Delta} + \frac{1}{(\omega+\omega_0)-\mathrm{i}\Delta} - \frac{1}{(\omega+\omega_0)+\mathrm{i}\Delta}\right]. \tag{C18}$$

Substituting this equation into Eq. (C17), we obtain

$$\begin{aligned} z_3 = \frac{1}{2}\Bigg\{&\frac{1}{2\pi\mathrm{i}}\int_{-\infty}^{\infty}\left[\frac{1}{(\omega-\omega_0)-\mathrm{i}\Delta} - \frac{1}{(\omega-\omega_0)+\mathrm{i}\Delta}\right]a^*(\omega,t)\,\mathrm{d}\omega \\ &+ \frac{1}{2\pi\mathrm{i}}\int_{-\infty}^{\infty}\left[\frac{1}{(\omega+\omega_0)-\mathrm{i}\Delta} - \frac{1}{(\omega+\omega_0)+\mathrm{i}\Delta}\right]a^*(\omega,t)\,\mathrm{d}\omega\Bigg\}. \end{aligned} \tag{C19}$$

The two integrals above can be evaluated using the residue method, using as a contour the infinite semicircle of the lower half plane, oriented clockwise. This yields $2\pi\mathrm{i}a^*(\pm\omega_0 - \mathrm{i}\Delta, t)$, where the positive sign holds for the first integral and the negative one for the second. Substituting this into the equation above, we obtain

$$z_3 = \tfrac{1}{2}(a^*(\omega_0 - \mathrm{i}\Delta, t) + a^*(-\omega_0 - \mathrm{i}\Delta, t)). \tag{C20}$$

Introducing the partial third-order parameters $z_{3+} = a^*(\omega_0 - \mathrm{i}\Delta, t)$ and $z_{3-} = a^*(-\omega_0 - \mathrm{i}\Delta, t)$, we can rewrite the last equation as

$$z_3 = \frac{z_{3+} + z_{3-}}{2}. \tag{C21}$$

Substituting this into Eq. (C15) yields

$$\begin{aligned} \dot{z}_{3+} &= -\frac{3K}{2}\left(z_1^{*3}z_{3+}^2 - z_1^3\right) - 3(\Delta - \mathrm{i}\omega_0)z_{3+}, \\ \dot{z}_{3-} &= -\frac{3K}{2}\left(z_1^{*3}z_{3-}^2 - z_1^3\right) - 3(\Delta + \mathrm{i}\omega_0)z_{3-}, \end{aligned} \tag{C22}$$

which is the system in Eq. (10).

APPENDIX D: CALCULATION OF z_1 AS A FUNCTION OF z_3

To solve the system in Eq. (10), we need to find a relationship between z_1 and z_3 that closes the dynamical equations. We derive this relationship from theoretical calculations of the partial order parameters within each synchronous region and then solve it numerically. Specifically, we first derive the relationship between the partial order parameters $z_{1,p}$ and $z_{3,p}$ for a stable system with symmetric unimodal natural frequency distribution centered at 0. Then, assuming that the two peaks in the bimodal system are dynamically independent, we apply this relationship to derive the connection between the global order parameters z_1 and z_3. The detailed derivation is presented below.

Consider oscillators that are phase locked within a single stable region $\theta \in [\frac{\beta}{3} - \frac{\pi}{6}, \frac{\beta}{3} + \frac{\pi}{6}]$. Using $\Theta_1 - \beta = \frac{\Theta_3}{3}$ as reference, the dynamics of the oscillators is described by

$$\dot{\theta}_i = \omega_i - \Omega_1 - KR_1^3 \sin(3\theta_i - \beta), \tag{D1}$$

where Ω_1 is the angular velocity of the order parameter z_1. In the phase-locked state, $\dot{\theta}_i = 0$, and therefore

$$\omega_i = \Omega_1 + KR_1^3 \sin(3\theta_i - \beta). \tag{D2}$$

In the thermodynamic limit, this yields

$$\mathrm{d}\omega = 3KR_1^3 \cos(3\theta - \beta)\mathrm{d}\theta. \tag{D3}$$

Also, $\theta \in [\frac{\beta}{3} - \frac{\pi}{6}, \frac{\beta}{3} + \frac{\pi}{6}]$ corresponds to $\omega \in [\Omega_1 - KR_1^3, \Omega_1 + KR_1^3]$. Then, assuming a symmetric unimodal natural frequency distribution $g(\omega)$, centered at 0, the partial order parameters are

$$R_{1,p} = \int_{-KR_1^3}^{KR_1^3} \mathrm{e}^{\mathrm{i}\theta} g(\omega)\mathrm{d}\omega = 3KR_1^3 \int_{\frac{\beta}{3}-\frac{\pi}{6}}^{\frac{\beta}{3}+\frac{\pi}{6}} \cos\theta \cos(3\theta - \beta) g\big(KR_1^3 \sin(3\theta - \beta) + \Omega_1\big)\mathrm{d}\theta, \tag{D4}$$

$$R_{3,p} = \int_{-KR_1^3}^{KR_1^3} \mathrm{e}^{3\mathrm{i}\theta} g(\omega)\mathrm{d}\omega = 3KR_1^3 \int_{\frac{\beta}{3}-\frac{\pi}{6}}^{\frac{\beta}{3}+\frac{\pi}{6}} \cos(3\theta) \cos(3\theta - \beta) g\big(KR_1^3 \sin(3\theta - \beta) + \Omega_1\big)\mathrm{d}\theta. \tag{D5}$$

As can be seen from Fig. 2, under the new scaling all clusters collapse to the same position. This implies that the phase Θ_3 of the order parameter in this scale effectively describes the central position of the oscillators within each cluster. Consequently, we approximate Ω_1 as the angular velocity of an oscillator whose phase is exactly $\frac{\Theta_3}{3}$. Furthermore, since the locked region is centered around the peak of $g(\omega)$ at $\omega = 0$, we approximate the natural frequency of this representative oscillator as 0. Substituting $\theta_i = \frac{\Theta_3}{3}$ and $\omega_i = 0$ into Eq. (2) yields the specific relation $\Omega_1 \approx KR_1^3 \sin\beta$. Drifting oscillators are in a rotating state and their contribution to the order parameters is approximately 0. Then, we vary R_1 in [0, 1], compute the two integrals above, and obtain paired data $(R_{3,p}, R_{1,p})$. These data are then fitted to describe the relation $R_{1,p} = F(R_{3,p})$. This function F encapsulates the relationship between the partial first-order and third-order parameters for oscillators in each stable region. For the whole system, the first-order order parameter is obtained from the three clusters according to

$$z_1 = \sum_{p=0}^{2} \gamma_p z_{1,p} = \sum_{p=0}^{2} \gamma_p R_{1,p} \mathrm{e}^{\mathrm{i}\Theta_{1,p}}, \tag{D6}$$

where γ_p represents the proportion of oscillators belonging to the pth cluster. A key simplification then arises from the symmetry of the system. As mentioned above, if the oscillators have the same frequency distribution, their phase distributions in the stable regions are identical up to a constant phase shift of $\frac{2\pi}{3}$. This means that the partial nth order parameters in different regions have identical magnitudes $R_{n,p}$ and phase differences of $\frac{2n\pi}{3}$, where the factor of n is due to the scaling transformation. Thus, we can write

$$\Theta_{3,p} = \Theta_{3,0} + 2p\pi. \tag{D7}$$

Applying this to the third-order parameter, we obtain

$$z_3 = \sum_{p=0}^{2} \gamma_p z_{3,p} = \sum_{p=0}^{2} \gamma_p R_{3,p} \mathrm{e}^{\mathrm{i}(\Theta_{3,0}+2p\pi)} = R_{3,p} \mathrm{e}^{\mathrm{i}\Theta_{3,0}}. \tag{D8}$$

This result confirms that the global third-order phase is equal to the phase of the cluster, as are the magnitudes of the global third-order parameter and of the cluster third-order parameter. In formulas, $\Theta_3 = \Theta_{3,0}$ and $R_3 = R_{3,p}$. Furthermore, since the oscillators within each synchronization region form a single coherent cluster and do not exhibit any deflection effect, which requires an asymmetric distribution among multiple clusters, the phase of the first-order parameter for each cluster is simply $\Theta_{1,p} = \frac{\Theta_{3,p}}{3}$. Combined with the phase relationship of Eq. (D7), we obtain $\Theta_{1,p} = \frac{\Theta_3 + 2\pi p}{3}$. Substituting this and $R_{1,p} = F(R_3)$ into the expression for z_1 yields

$$\begin{aligned} z_1 &= \sum_{p=0}^{2} \gamma_p F(R_3) \mathrm{e}^{\mathrm{i}\frac{\Theta_3 + 2\pi p}{3}} \\ &= F(R_3) \mathrm{e}^{\mathrm{i}\frac{\Theta_3}{3}} \sum_{p=0}^{2} \gamma_p \mathrm{e}^{\mathrm{i}\frac{2\pi p}{3}} \\ &= F(R_3) C \mathrm{e}^{\mathrm{i}\frac{\Theta_3}{3}}, \end{aligned} \tag{D9}$$

where $C = \sum_{p=0}^{2} \gamma_p \mathrm{e}^{\mathrm{i}\frac{2p\pi}{3}}$ describes the phase distortion induced by the asymmetric distribution.

The bimodal distribution used in our treatment can be considered as a combination of two unimodal distributions. Since the two peaks are sufficiently separated in frequency, we treat the dynamics of the two peaks as approximately independent, and the partial order parameters for each peak are expected

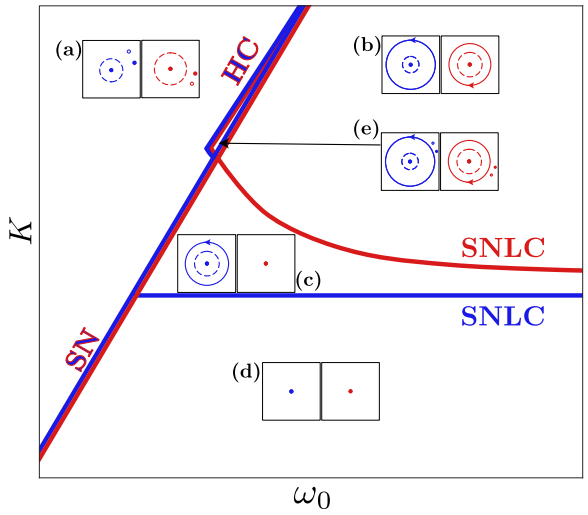

FIG. 7. The phase boundaries in the diagram of Fig. 4(a) correspond to three different types of bifurcation. Panels (a)–(d) represent four typical dynamical states of the system: (a) synchronized state, (b) standing-wave state, (c) chimera state, and (d) incoherent state. Panel (e) represents the coexistence of the standing-wave and synchronized states. Blue and red denote the two order parameters z_+ and z_-, respectively. Solid (hollow) dots represent stable (unstable) fixed points and solid (dashed) circles correspond to stable (unstable) limit cycles. The bifurcation types are saddle node (SN), saddle node of limit cycles (SNLC), and homoclinic (HC).

to follow the same functional relationship derived for the unimodal case and given by Eq. (D9). Thus,

$$z_{1+} = F(R_{3+})Ce^{i\frac{\Theta_{3+}}{3}}, \tag{D10}$$

$$z_{1-} = F(R_{3-})Ce^{i\frac{\Theta_{3-}}{3}}, \tag{D11}$$

where $R_{3\pm}$ and $\Theta_{3\pm}$ are the amplitude and phase of $z_{3\pm}$. The constant C is the same for both peaks because the relative distribution of oscillators among the three clusters within each peak is identical, so that $\gamma_{p+} = \gamma_{p-}$ for all p. The global order parameter is then obtained by averaging the contributions from the two subpopulations, using

$$\begin{aligned} z_1 &= \tfrac{1}{2}(z_{1+} + z_{1-}) \\ &= \tfrac{1}{2}\left(F(R_{3+})Ce^{i\frac{\Theta_{3+}}{3}} + F(R_{3-})Ce^{i\frac{\Theta_{3-}}{3}}\right). \end{aligned} \tag{D12}$$

In the numerical integration of Eq. (10), we close the dynamical system by substituting this relation for z_1 as a function of z_3 at each time step.

APPENDIX E: BIFURCATION ANALYSIS

The theoretical analysis yields a set of dynamical equations involving two complex variables, $z_{3\pm}$, which contain numerically fitted functions. These terms make it difficult to perform a rigorous analytical bifurcation analysis. Therefore, taking the case shown in Fig. 4(a) as an example, we analyze the bifurcation behavior by examining the dynamics of $z_{3\pm}$ in a rotating frame defined by $z_{3\mp}$, as illustrated in Fig. 7. This approach, validated by direct numerical simulations, allows us to reconstruct the essential bifurcation diagram.

Figure 7 shows five representative dynamical states of the system and their transitions, namely, the synchronized state [panel (a)], the standing-wave state [panel (b)], the chimera state [panel (c)], and the incoherent state [panel (d)], as well as a very small tristable region [panel (e)]. In this region [panel (e)], our analysis predicts the coexistence of a stable fixed point (synchronized state) and a limit cycle (standing-wave state). However, this limit cycle is, in fact, unstable. Because of the limitations of our theoretical analysis, the system is inevitably driven away from this unstable orbit and transitions to the stable chimera state [panel (c)]. Thus, this region is not observed in the phase diagram shown in the Fig. 4.

The blue and red colors denote the order parameters z_{3+} and z_{3-}, respectively. Solid dots represent stable fixed points, hollow dots represent unstable fixed points, solid circles correspond to stable limit cycles, and dashed circles correspond to

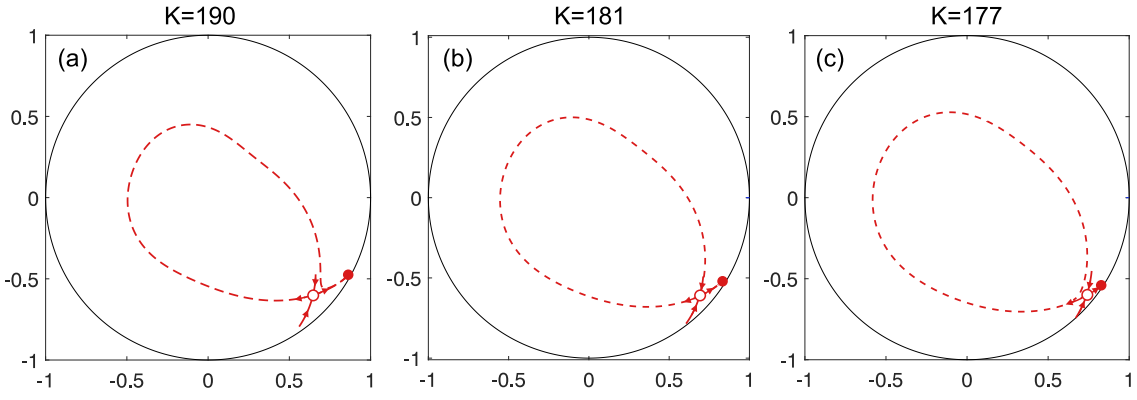

FIG. 8. Formation of limit cycles near the homoclinic bifurcation. The synchronized manifold of z_{3-} is plotted in the reference frame of z_{3+} for $\omega_0 = 70$ at different coupling strengths K. The phase is divided by 3 for clarity. Hollow circles indicate saddle points. Dashed lines indicate unstable manifolds, computed by forward integration (Euler method) of initial conditions displaced along the unstable eigenvector. Solid lines indicate stable manifolds, computed by backward integration along the stable eigenvector. Solid dots indicate stable fixed points. (a) At $K = 190$, before the bifurcation, the unstable and stable manifolds do not intersect, and no limit cycle exists. (b) At $K = 181$, near the critical point, the unstable and stable manifolds nearly coincide, forming a limit cycle. (c) At $K = 177$, after the bifurcation, the unstable manifold forms a closed curve, indicating the formation of a limit cycle.

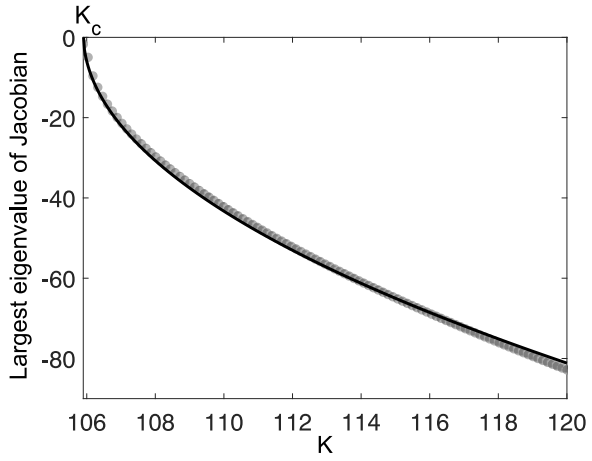

FIG. 9. The convergence of the leading eigenvalue of the Jacobian shows the emergence of a saddle node bifurcation. The largest nontrivial eigenvalue of the Jacobian matrix, evaluated at the stable fixed point, is plotted against the coupling strength K for $\omega_0 = 40$. As the system approaches the SN bifurcation point ($K_c \approx 105.9$), this eigenvalue approaches 0, characteristic of the collision and annihilation of a stable and an unstable fixed point.

unstable limit cycles. When plotting z_{3+} (blue), the direction of z_{3-} is taken as the reference frame, and when plotting z_{3-} (red), the direction of z_{3+} is taken as the reference frame, each showing a projection of the system dynamics. For cases where the magnitude of z_{3+} (z_{3-}) approaches 0, the phase loses its meaning, so the original reference frame is chosen when plotting z_{3-} (z_{3+}).

When the system transitions from the synchronized state [panel (a)] to state [panel (e)], a homoclinic (HC) bifurcation occurs. In this process, oscillators that moved away from the unstable manifold of the saddle point (hollow dot) return to it along the stable manifold, forming a limit cycle, as shown in Fig. 8. The stable and unstable manifolds of the saddle point in the figure were computed numerically using the standard Euler method to integrate the dynamical equations forward and backward in time along the corresponding eigenvectors, respectively.The transition from the synchronized state [panel (a)] to states (b), (c), or (d) occurs via an SN bifurcation. Figure 9 demonstrates this by showing the dominant eigenvalue of the Jacobian matrix associated with the stable fixed point. This is achieved by first solving for the fixed point x^* in the Θ_{3-} rotating frame across a range of values of K, and then evaluating the Jacobian of the resulting two-dimensional subsystem (for z_{3+}, with z_{3-} fixed) at x^* using a central finite-difference method. The convergence of the leading real eigenvalue toward 0 serves as a numerical signature of the impending saddle-node bifurcation.

When the system changes from the standing-wave state [panel (b)] to the chimera state [panel (c)], z_{3-} undergoes a saddle node of limit cycles (SNLC) bifurcation, in which the stable and unstable limit cycles merge and vanish, resulting in z_{3-} approaching 0. The evidence for this is that an estimate of the dominant Floquet multiplier approaches 1 at the transition point, as shown in Fig. 10(a). This estimate was obtained by perturbing the stable limit cycle (found using the Euler method) and quantifying the rate of exponential convergence of the trajectory back to the cycle over subsequent periods, effectively capturing the multiplier governing the SNLC bifurcation. Finally, as the chimera state [panel (c)] evolves toward the incoherent state [panel (d)], z_{3+} also experiences an SNLC bifurcation, where the stable and unstable limit cycles collide and disappear. The evidence for this is similar to that of z_{3-}, as shown in Fig. 10(b), and the system eventually enters an incoherent state.

APPENDIX F: OTHER INTERACTION ORDERS

For our treatment, we focused on a pure four-body model as a minimal, analytically transparent description of the mechanism valid when the four-body coupling dominates (K_2, $K_3 \to 0$). Here, we examine how lower-order terms affect the phenomenon by adding a pairwise (first-order) coupling with strength K_1 and a three-body (second-order) coupling with

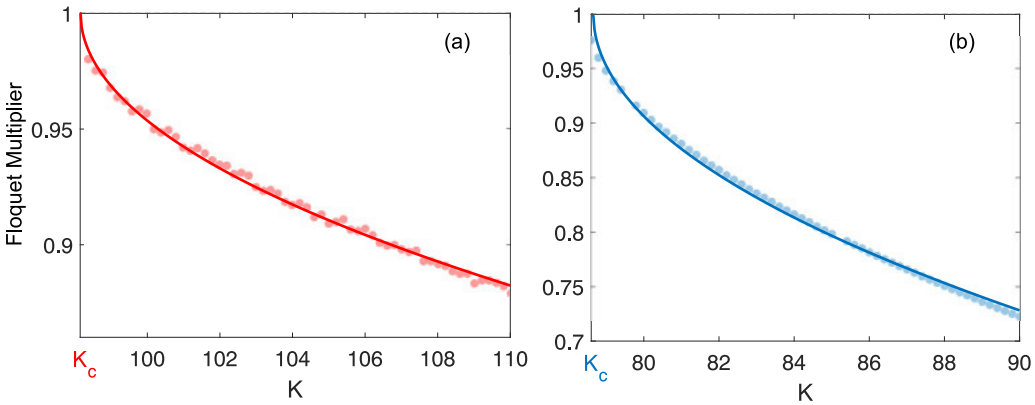

FIG. 10. The convergence of the Floquet multipliers provides evidence for the emergence of saddle node of limit cycles bifurcations. The evolution of the estimated dominant Floquet multiplier for the limit cycles of z_{3-} and z_{3+} is shown for $\omega_0 = 100$. The estimate was obtained by applying a small perturbation to the stable limit cycle (found via the Euler method) and computing the rate of exponential convergence of the trajectory over some periods. This rate provides a direct measure of the magnitude of the dominant Floquet multiplier. (a) For z_{3-} at $K_c \approx 98.1$, the multiplier approaches $+1$, signaling an SNLC bifurcation. (b) A similar behavior is found for z_{3+} at $K_c \approx 78.6$. The fitted curves are guides for the eye.

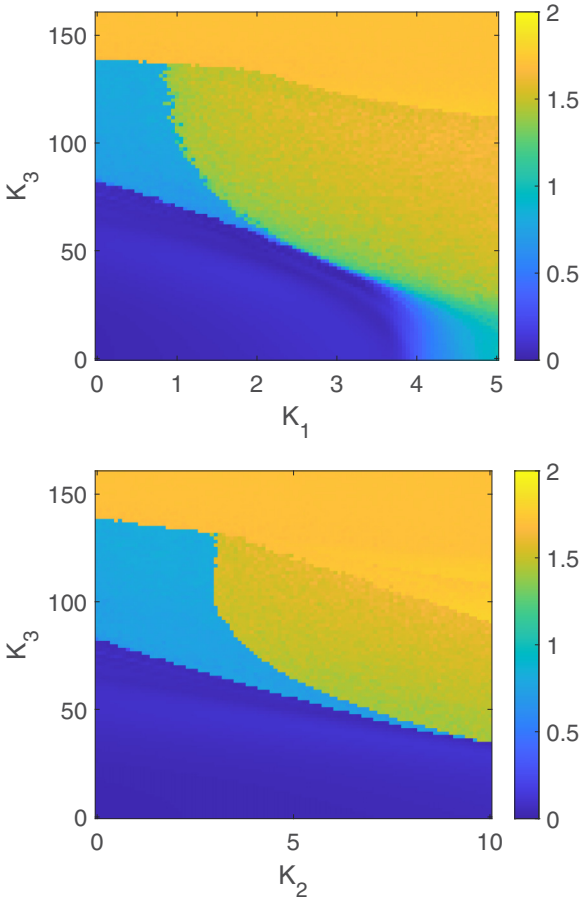

FIG. 11. The chimera state induced by intrinsic frustration is robust with respect to the presence of lower-order interactions. The values of $R^+ + R^-$ at steady state show the chimera state emerging even in the presence of first-order (left) and second-order (right) interactions, so long as they do not completely dominate the system. In the left-hand panel, the second-order coupling K_2 is set to 0; in the right-hand panel, the first-order coupling K_1 is set to 0. Both panels show the state of the system at time $T = 20$. The simulations used 1000 oscillators, integration step 10^{-3}, Lorentzian frequency distribution with width $\Delta = 1$, and initial phases set at 0, $2\pi/3$, and $4\pi/3$ with population ratio $9:1:0$.

strength K_2. Then, the equation of the system becomes

$$\dot{\theta}_i = \omega_i + \frac{K_1}{N}\sum_j \sin(\theta_j - \theta_i) + \frac{K_2}{N^2}\sum_{j,k}\sin(\theta_j + \theta_k - 2\theta_i) + \frac{K_3}{N^3}\sum_{j,k,l}\sin(\theta_j + \theta_k + \theta_l - 3\theta_i). \tag{F1}$$

Introducing the complex order parameter $z = Re^{i\Theta} = \frac{1}{N}\sum_{j=1}^{N} e^{i\theta_j}$, the dynamics reduce to

$$\dot{\theta}_i = \omega_i - K_1 R\sin(\theta_i - \Theta) - K_2 R^2 \sin(2(\theta_i - \Theta)) - K_3 R^3 \sin(3(\theta_i - \Theta)). \tag{F2}$$

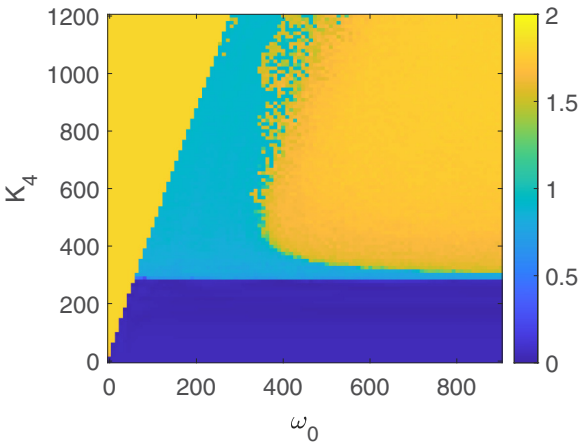

FIG. 12. The chimera state induced by intrinsic frustration emerges for interaction orders greater than 3. The values of $R^+ + R^-$ at steady state show the chimera state emerging also in the fourth-order model. The state of the system is shown at time $T = 20$. The simulations used 1000 oscillators, integration step 10^{-4}, Lorentzian frequency distribution with width $\Delta = 1$, and initial phases set at 0, $\pi/2$, π, and $3\pi/2$ with population ratio $9:1:0:0$.

Assigning the initial phases of the oscillators to be 0, $2\pi/3$, and $4\pi/3$ with population ratio $9:1:0$, and fixing $\omega_0 = 50$, we carried out numerical simulations to quantify the difference in synchronization levels between the two groups of oscillators for different values of the coupling strengths K_1, K_2, and K_3. The results, illustrated in Fig. 11, show that when the lower-order couplings are weak enough, increasing them lowers the threshold value of K_3 at which the chimera state emerges. Mechanistically, pairwise or triadic interactions increase the mobility of oscillators across multiple fixed points, so the two frequency-symmetric groups acquire an asymmetric phase distributions. This erodes the symmetry present in the initial distribution and amplifies the dynamical asymmetry. When the lower-order coupling K_1 or K_2 becomes strong enough, it controls the fixed-point distribution, suppressing the intrinsic frustration generated by the presence of multiple fixed points. As a result, the associated symmetry breaking disappears and the system settles into a standing-wave or a fully synchronized state.

The dynamical asymmetry described above is not limited to triadic couplings. In fact, it also arises for interaction orders higher than 3. As a concrete example, consider the fourth-order Kuramoto model,

$$\dot{\theta}_i = \omega_i + \frac{K_4}{N^4}\sum_{j_1,j_2,j_3,j_4=1}^{N}\sin(\theta_{j_1} + \theta_{j_2} + \theta_{j_3} + \theta_{j_4} - 4\theta_i). \tag{F3}$$

The dynamics of this model is described by

$$\dot{\theta}_i = \omega_i - K_4 R^4 \sin(4(\theta_i - \Theta)). \tag{F4}$$

This system possesses four fixed points, equally spaced on the circle. We initialize oscillators at these four fixed points with an asymmetric ratio $9:1:0:0$ and directly solve Eq. (F4), finding the emergence of a chimera state, as reported in Fig. 12.

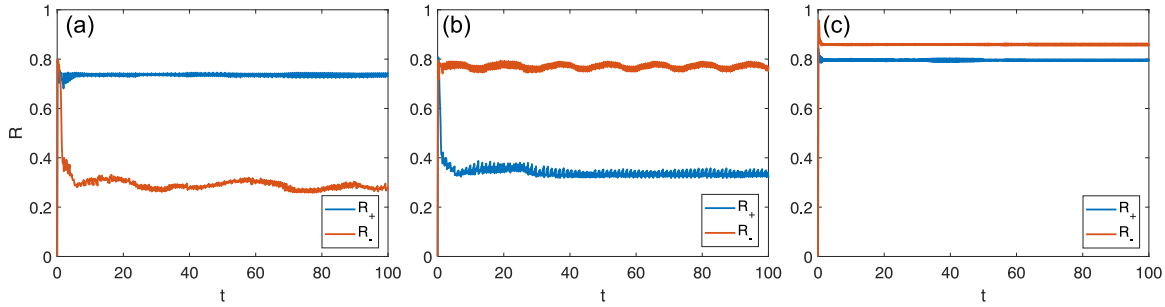

FIG. 13. Dynamical asymmetry arises even in Erdős-Rényi random networks. The partial order parameters of the two subpopulations of oscillators associated with the positive and negative frequency peaks, R^+ and R^-, show the existence of a dynamical asymmetry in the third-order Kuramoto model on Erdős-Rényi graphs for asymmetric initial conditions. The coupling strength used is $K = 25$, the peaks of the natural frequency distribution are centered at ± 5, the width of the peaks is $\Delta = 0.1$, the numerical integration step is 0.1, and the initial phases are placed at three equidistant points on the circle, namely, 0, $2\pi/3$, and $4\pi/3$. Panel (a) has a starting population ratio $9:1:0$, for which the positively rotating group attains stronger synchrony. The ratio in panel (b) is $9:0:1$, for which the negatively rotating group attains stronger synchrony. The ratio for panel (c) is $1:0:0$, for which the two groups exhibit comparable synchrony.

These results show that, for interaction orders greater than or equal to 3, an asymmetry in the initial phase distribution can lead to dynamical asymmetry regardless of the presence of lower-order interactions.

APPENDIX G: DIFFERENT NETWORK TOPOLOGIES

To show that the emergence of the chimera state is robust with respect to the network topology, we studied the model on random graphs and on a real-world biological network.

1. Erdős-Rényi random graphs

To test the results on random networks, we generated an Erdős-Rényi graph with connection probability $p = 0.5$ and $N = 200$ nodes, treating each 4-clique as a four-body interaction. Defining H to be the indicator variable such that $H_{i,j,k,l} = 1$ if nodes i, j, k, and l form a clique, and 0 otherwise, the dynamics are given by

$$\dot{\theta}_i = \omega_i + \frac{K}{N_i} \sum_{j<k<l} H_{i,j,k,l} \sin(\theta_j + \theta_k + \theta_l - 3\theta_i). \quad \text{(G1)}$$

Drawing the natural frequencies from a symmetric bimodal Lorentzian distribution with peaks at $\pm\omega_0$ of width Δ, we use $\mathcal{G}_\pm$ to denote the two frequency-symmetric groups, so that $\mathcal{G}_+$ is the set consisting of all the oscillators whose natural frequency was drawn from the Lorentzian peak at $+\omega_0$, and $\mathcal{G}_-$ is the one of all the oscillators whose frequency was drawn from the peak centered at $-\omega_0$. Then, we quantify the coherence for the two groups by defining

$$z_\pm(t) = \frac{1}{N_\pm} \sum_{i \in \mathcal{G}_\pm} e^{i\theta_i(t)} \quad \text{(G2)}$$

and $R_\pm = |z_\pm|$. The results of the simulations of the system, reported in Fig. 13, show that the degree of synchrony between oscillators rotating in the two opposite directions depends on the initial conditions, even though the natural frequency distribution is symmetric.

2. Brain network

Next, we performed the same procedure on a structural brain network with 998 nodes [54–56], treating each 4-clique as a four-body interaction. Using the empirical adjacency

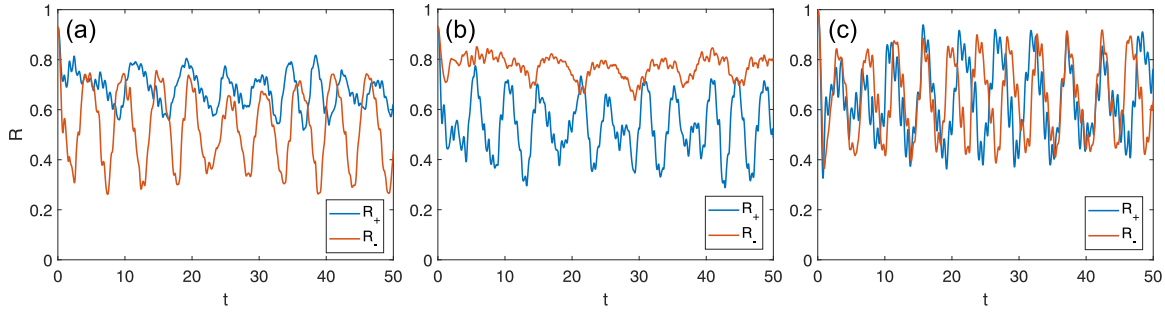

FIG. 14. Dynamical asymmetry arises on a brain network. The partial order parameters of the two subpopulations of oscillators associated with the positive and negative frequency peaks, R^+ and R^-, show the existence of a dynamical asymmetry in the third-order Kuramoto model on a structural brain network for asymmetric initial conditions. The pairwise coupling strength used is $K_1 = 3$, the four-body one is $K_3 = 15$, the peaks of the natural frequency distribution are centered at ± 5, the width of the peaks is $\Delta = 0.1$, the numerical integration step is 0.01, and the initial phases are placed at three equidistant points on the circle, namely, 0, $2\pi/3$, and $4\pi/3$. Panel (a) has a starting population ratio $9:1:0$, for which the positively rotating group attains stronger synchrony. The ratio in panel (b) is $9:0:1$, for which the negatively rotating group attains stronger synchrony. The ratio for panel (c) is $1:0:0$, for which the two groups exhibit comparable synchrony.

matrix $\mathbf{A}$, we added a pairwise coupling strength K_1 for the four-body term, resulting in the evolution equation

$$\dot{\theta}_i = \omega_i + \frac{K_3}{N_i}\sum_{j<k<l} H_{i,j,k,l}\sin(\theta_j+\theta_k+\theta_l-3\theta_i) + \frac{K_1}{d_i}\sum_j A_{i,j}\sin(\theta_j-\theta_i), \tag{G3}$$

where d_i is the degree of node i. With the same symmetric bimodal Lorentzian distribution of natural frequencies, we again computed $z_\pm$ and $R_\pm$ and found the different coherence levels between the two groups. These results, illustrated in Fig. 14, confirm that the effect is not restricted to globally coupled networks. In fact, as long as the higher-order interactions are sufficiently strong, the same symmetry-breaking behavior appears also on more general complex networks.

APPENDIX H: MORE GENERAL INITIAL CONDITIONS

In the case we analyzed in detail, the oscillators were initialized at three discrete phases, 0, $2\pi/3$, and $4\pi/3$, with specific population ratios. Here, we relax this assumption by adding random phase offsets $\Delta\theta \in [-\pi/3, \pi/3]$ to each group, so that oscillators are distributed within three angular sectors of width $2\pi/3$ on the unit circle while preserving the same ratios. Direct simulations, whose results are illustrated in Fig. 15, show that the chimera state persists under this sector-wise continuous initialization. This demonstrates that the phenomenon does not rely on point-mass initial conditions and is robust to broader, more realistic phase ensembles.

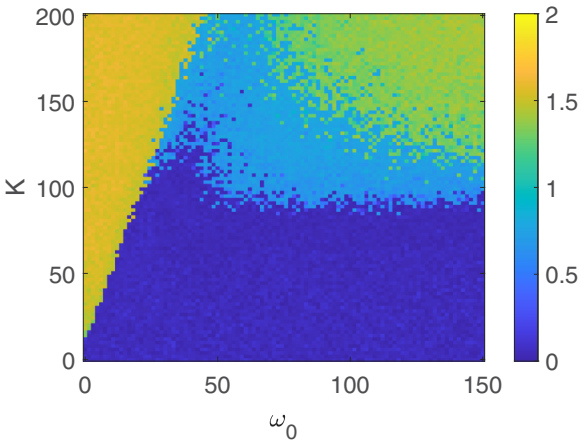

FIG. 15. The chimera state induced by intrinsic frustration is robust with respect to changes in initial conditions. The values of $R^+ + R^-$ at steady state show the chimera state emerging also when the initial phases of the oscillators in each group are not identical, but are uniformly distributed over an interval of width $2\pi/3$. The state of the system is shown at time $T = 20$. The simulations used 1000 oscillators, integration step 10^{-4}, Lorentzian frequency distribution with width $\Delta = 1$, and initial phases with population ratio $9:1:0$.

[1] J. M. Levine, J. Bascompte, P. B. Adler, and S. Allesina, Beyond pairwise mechanisms of species coexistence in complex communities, Nature (London) **546**, 56 (2017).

[2] J. Grilli, G. Barabás, M. J. Michalska-Smith, and S. Allesina, Higher-order interactions stabilize dynamics in competitive network models, Nature (London) **548**, 210 (2017).

[3] M. Perc, J. J. Jordan, D. G. Rand, Z. Wang, S. Boccaletti, and A. Szolnoki, Statistical physics of human cooperation, Phys. Rep. **687**, 1 (2017).

[4] U. Alvarez-Rodriguez, F. Battiston, G. Ferraz de Arruda, Y. Moreno, M. Perc, and V. Latora, Evolutionary dynamics of higher-order interactions in social networks, Nat. Hum. Behav. **5**, 586 (2021).

[5] R. Sahasrabuddhe, L. Neuhäuser, and R. Lambiotte, Modelling non-linear consensus dynamics on hypergraphs, J. Phys. Complexity **2**, 025006 (2021).

[6] E. Ganmor, R. Segev, and E. Schneidman, Sparse low-order interaction network underlies a highly correlated and learnable neural population code, Proc. Natl. Acad. Sci. USA **108**, 9679 (2011).

[7] G. Petri, P. Expert, F. Turkheimer, R. Carhart-Harris, D. Nutt, P. J. Hellyer, and F. Vaccarino, Homological scaffolds of brain functional networks, J. R. Soc. Interface **11**, 20140873 (2014).

[8] F. A. N. Santos, E. P. Raposo, M. D. Coutinho-Filho, M. Copelli, C. J. Stam, and L. Douw, Topological phase transitions in functional brain networks, Phys. Rev. E **100**, 032414 (2019).

[9] A. R. Benson, R. Abebe, M. T. Schaub, A. Jadbabaie, and J. Kleinberg, Simplicial closure and higher-order link prediction, Proc. Natl. Acad. Sci. USA **115**, 11221 (2018).

[10] F. Battiston, G. Cencetti, I. Iacopini, V. Latora, M. Lucas, A. Patania, J.-G. Young, and G. Petri, Networks beyond pairwise interactions: Structure and dynamics, Phys. Rep. **874**, 1 (2020).

[11] S. Boccaletti, P. De Lellis, C. I. del Genio, K. Alfaro-Bittner, R. Criado, S. Jalan, and M. Romance, The structure and dynamics of networks with higher order interactions, Phys. Rep. **1018**, 1 (2023).

[12] P. S. Skardal, E. Ott, and J. G. Restrepo, Cluster synchrony in systems of coupled phase oscillators with higher-order coupling, Phys. Rev. E **84**, 036208 (2011).

[13] M. H. Matheny, J. Emenheiser, W. Fon, A. Chapman, A. Salova, M. Rohden, J. Li, M. Hudoba de Badyn, M. Pósfai, L. Duenas-Osorio, M. Mesbahi, J. P. Crutchfield, M. C. Cross, R. M. D'Souza, and M. L. Roukes, Exotic states in a simple network of nanoelectromechanical oscillators, Science **363**, eaav7932 (2019).

[14] Y. Zhang, V. Latora, and A. E. Motter, Unified treatment of synchronization patterns in generalized networks with higher-order, multilayer, and temporal interactions, Commun. Phys. **4**, 195 (2021).

[15] S. Kundu and D. Ghosh, Higher-order interactions promote chimera states, Phys. Rev. E **105**, L042202 (2022).

[16] X. Li, M. Small, and Y. Lei, Reservoir computing with higher-order interactive coupled pendulums, Phys. Rev. E **108**, 064304 (2023).
[17] E. T. K. Mau, O. Omel'chenko, and M. Rosenblum, Phase reduction explains chimera shape: When multibody interaction matters, Phys. Rev. E **110**, L022201 (2024).
[18] X. Ji and X. Li, Chimera-inspired dynamics: When higher-order interactions are expressed differently, Phys. Rev. E **110**, 044204 (2024).
[19] D. M. Abrams and S. H. Strogatz, Chimera states for coupled oscillators, Phys. Rev. Lett. **93**, 174102 (2004).
[20] F. Parastesh, S. Jafari, H. Azarnoush, Z. Shahriari, Z. Wang, S. Boccaletti, and M. Perc, Chimeras, Phys. Rep. **898**, 1 (2021).
[21] S. W. Haugland, The changing notion of chimera states, a critical review, J. Phys. Complex. **2**, 032001 (2021).
[22] C. R. Laing, Chimera states in heterogeneous networks, Chaos **19**, 013113 (2009).
[23] C. R. Laing, The dynamics of chimera states in heterogeneous Kuramoto networks, Physica D **238**, 1569 (2009).
[24] C. R. Laing, K. Rajendran, and I. G. Kevrekidis, Chimeras in random non-complete networks of phase oscillators, Chaos **22**, 013132 (2012).
[25] M. R. Tinsley, S. Nkomo, and K. Showalter, Chimera and phase-cluster states in populations of coupled chemical oscillators, Nat. Phys. **8**, 662 (2012).
[26] S. Nkomo, M. R. Tinsley, and K. Showalter, Chimera states in populations of nonlocally coupled chemical oscillators, Phys. Rev. Lett. **110**, 244102 (2013).
[27] J. Shena, J. Hizanidis, V. Kovanis, and G. P. Tsironis, Turbulent chimeras in large semiconductor laser arrays, Sci. Rep. **7**, 42116 (2017).
[28] T. Makinwa, K. Inaba, T. Inagaki, Y. Yamada, T. Leleu, T. Honjo, T. Ikuta, K. Enbutsu, T. Umeki, R. Kasahara, K. Aihara, and H. Takesue, Experimental observation of chimera states in spiking neural networks based on degenerate optical parametric oscillators, Commun. Phys. **6**, 121 (2023).
[29] L. V. Gambuzza, A. Buscarino, S. Chessari, L. Fortuna, R. Meucci, and M. Frasca, Experimental investigation of chimera states with quiescent and synchronous domains in coupled electronic oscillators, Phys. Rev. E **90**, 032905 (2014).
[30] T. Yamaguchi, Stacking fault and four-body interaction in the Si(111)7 × 7 structure, Phys. Rev. B **34**, 1085 (1986).
[31] M. Horoi, Staggering of the nuclear charge radii in a superfluid model with good particle number, Phys. Rev. C **50**, 2834 (1994).
[32] J. Han, Five-body van der Waals interactions, Phys. Rev. A **95**, 062502 (2017).
[33] T. Tanaka and T. Aoyagi, Multistable attractors in a network of phase oscillators with three-body interactions, Phys. Rev. Lett. **106**, 224101 (2011).
[34] C. Bick, P. Ashwin, and A. Rodrigues, Chaos in generically coupled phase oscillator networks with nonpairwise interactions, Chaos **26**, 094814 (2016).
[35] P. S. Skardal and A. Arenas, Abrupt desynchronization and extensive multistability in globally coupled oscillator simplexes, Phys. Rev. Lett. **122**, 248301 (2019).
[36] I. León and D. Pazó, Enlarged Kuramoto model: Secondary instability and transition to collective chaos, Phys. Rev. E **105**, L042201 (2022).
[37] I. León, R. Muolo, S. Hata, and H. Nakao, Higher-order interactions induce anomalous transitions to synchrony, Chaos **34**, 013105 (2024).
[38] P. Ashwin and A. Rodrigues, Hopf normal form with S_N symmetry and reduction to systems of nonlinearly coupled phase oscillators, Physica D **325**, 14 (2016).
[39] K. Kovalenko, X. Dai, K. Alfaro-Bittner, A. M. Raigorodskii, M. Perc, and S. Boccaletti, Contrarians synchronize beyond the limit of pairwise interactions, Phys. Rev. Lett. **127**, 258301 (2021).
[40] Z. Cai, Z. Liu, S. Guan, J. Kurths, and Y. Zou, High-mode coupling yields multicoherent-phase phenomena in nonlocally coupled oscillators, Phys. Rev. Lett. **133**, 227201 (2024).
[41] C. Mitra, A. Choudhary, S. Sinha, J. Kurths, and R. V. Donner, Multiple-node basin stability in complex dynamical networks, Phys. Rev. E **95**, 032317 (2017).
[42] S. Khan and H. E. Türeci, Frequency combs in a lumped-element Josephson-junction circuit, Phys. Rev. Lett. **120**, 153601 (2018).
[43] A. F. Taylor, P. Kapetanopoulos, B. J. Whitaker, R. Toth, L. Bull, and M. R. Tinsley, Clusters and switchers in globally coupled photochemical oscillators, Phys. Rev. Lett. **100**, 214101 (2008).
[44] A. F. Taylor, M. R. Tinsley, F. Wang, and K. Showalter, Phase clusters in large populations of chemical oscillators, Angew. Chem. Int. Ed **50**, 10161 (2011).
[45] A. Navas-Olive, M. Valero, T. Jurado-Parras, A. de Salas-Quiroga, R. G. Averkin, G. Gambino, E. Cid, and L. M. de la Prida, Multimodal determinants of phase-locked dynamics across deep-superficial hippocampal sublayers during theta oscillations, Nat. Commun. **11**, 2217 (2020).
[46] A. Czurkó, J. Huxter, Y. Li, B. Hangya, and R. U. Muller, Theta phase classification of interneurons in the hippocampal formation of freely moving rats, J. Neurosci. **31**, 2938 (2011).
[47] J. E. Quintero, S. J. Kuhlman, and D. G. McMahon, The biological clock nucleus: A multiphasic oscillator network regulated by light, J. Neurosci. **23**, 8070 (2003).
[48] S. Ramans-Harborough, A. P. Kalverda, I. W. Manfield, G. S. Thompson, M. Kieffer, V. Uzunova, M. Quareshy, J. M. Prusinska, S. Roychoudhry, K.-I. Hayashi, R. Napier, C. del Genio, and S. Kepinski, Intrinsic disorder and conformational coexistence in auxin coreceptors, Proc. Natl. Acad. Sci. USA **120**, e2221286120 (2023).
[49] E. Ott and T. M. Antonsen, Low dimensional behavior of large systems of globally coupled oscillators, Chaos **18**, 037113 (2008).
[50] E. Ott and T. M. Antonsen, Long time evolution of phase oscillator systems, Chaos **19**, 023117 (2009).
[51] E. A. Martens, E. Barreto, S. H. Strogatz, E. Ott, P. So, and T. M. Antonsen, Exact results for the Kuramoto model with a bimodal frequency distribution, Phys. Rev. E **79**, 026204 (2009).
[52] H. Sakaguchi and Y. Kuramoto, A soluble active rotator model showing phase transitions via mutual entrainment, Prog. Theor. Phys. **76**, 576 (1986).
[53] https://github.com/zrguo-complexnet/IntrinsicFrustration.
[54] P. Hagmann, L. Cammoun, X. Gigandet, R. Meuli, C. J. Honey, V. J. Wedeen, and O. Sporns, Mapping the structural core of human cerebral cortex, PLoS Biol. **6**, e159 (2008).

[55] C. J. Honey, O. Sporns, L. Cammoun, X. Gigandet, J. P. Thiran, R. Meuli, and P. Hagmann, Predicting human resting-state functional connectivity from structural connectivity, Proc. Natl. Acad. Sci. USA **106**, 2035 (2009).

[56] S. Huo, C. Tian, M. Zheng, S. Guan, C. Zhou, and Z. Liu, Spatial multi-scaled chimera states of cerebral cortex network and its inherent structure-dynamics relationship in human brain, Natl. Sci. Rev. **8**, nwaa125 (2021).